

NIMS-PL: A Cable-Driven Robot With Self-Calibration Capabilities

Per Henrik Borgstrom, Brett L. Jordan, Bengt J. Borgstrom, *Member, IEEE*, Michael J. Stealey, Gaurav S. Sukhatme, *Senior Member, IEEE*, Maxim A. Batalin, *Member, IEEE*, and William J. Kaiser, *Senior Member, IEEE*

Abstract—We present the Networked InfoMechanical System for Planar Translation, which is a novel two-degree-of-freedom (2-DOF) cable-driven robot with self-calibration and online drift-correction capabilities. This system is intended for actuated sensing applications in aquatic environments. The actuation redundancy resulting from in-plane translation driven by four cables results in an infinite set of tension distributions, thus requiring real-time computation of optimal tension distributions. To this end, we have implemented a highly efficient, iterative linear programming solver, which requires a very small number of iterations to converge to the optimal value. In addition, two novel self-calibration methods have been developed that leverage the robot's actuation redundancy. The first uses an incremental displacement, or jitter method, whereas the second uses variations in cable tensions to determine end-effector location. We also propose a novel least-squares drift-detection algorithm, which enables the robot to detect long-term drift. Combined with self-calibration capabilities, this drift-monitoring algorithm enables long-term autonomous operation. To verify the performance of our algorithms, we have performed extensive experiments in simulation and on a real system.

Index Terms—Cable-driven robots, calibration and identification, field robots, parallel robots, redundant robots.

I. INTRODUCTION

CABLE-DRIVEN robots consist of computer-driven actuators that enable controlled release of cables. These cables, in turn, may support a variety of end-effector systems. Riechel

Manuscript received February 26, 2009; revised May 8, 2009. First published July 7, 2009; current version published October 9, 2009. This paper was recommended for publication by Associate Editor H. R. Choi and Editor W. K. Chung upon evaluation of the reviewers' comments. This work was supported in part by the U.S. National Science Foundation (NSF) under Grant ANI-00331481 and Grant ECCS-0725441. Any opinions, findings, and conclusions or recommendations expressed in this material are those of the authors and do not necessarily reflect the views of the NSF.

P. H. Borgstrom, B. J. Borgstrom, and W. J. Kaiser are with the Department of Electrical Engineering, University of California at Los Angeles, Los Angeles, CA 90095 USA (e-mail: henrik@ee.ucla.edu; jonas@ee.ucla.edu; kaiser@ee.ucla.edu).

B. L. Jordan is with the Department of Mechanical Engineering, University of California at Los Angeles, Los Angeles, CA 90095 USA (e-mail: bjordan5@gmail.com).

M. J. Stealey is with the Department of Electrical Engineering, University of California at Los Angeles, Los Angeles, CA 90095 USA, and also with the Renaissance Computing Institute, Chapel Hill, NC 27517 USA (e-mail: stealey@ucla.edu).

G. S. Sukhatme is with the Department of Computer Science, University of Southern California, Los Angeles, CA 90089 USA (e-mail: gaurav@usc.edu).

M. A. Batalin is with the Center for Embedded Networked Sensing, University of California at Los Angeles, Los Angeles CA 90024 USA (e-mail: maxim.batalin@cens.ucla.edu).

Color versions of one or more of the figures in this paper are available online at <http://ieeexplore.ieee.org>.

Digital Object Identifier 10.1109/TRO.2009.2024792

et al. [1] describe several advantages of cable-driven robots, including

- 1) remote location of motors and controls;
- 2) rapid deployability;
- 3) potentially large workspaces;
- 4) high load capacity;
- 5) reliability.

A balloon-cable-driven robot for use in search and rescue is developed in [2] but suffers from poor stability in windy conditions [3]. Additionally, several cable-driven robotic systems such as the SkyCam [4] and Cablecam [5] have found success in the fields of sports and entertainment. Similar platforms have been implemented for use as aerial vehicle simulators [6]. Recently, cable-based robotic systems have demonstrated critical capabilities for monitoring terrestrial [7] and aquatic [8]–[10] environments.

There is much prior work in kinematic, static, and dynamic analysis of cable-driven robotic systems. The authors of [11] present necessary and sufficient conditions for static equilibrium and derive conditions for completely restraining the robot. The conditions hinge on the existence of a strictly positive vector in the left null space of the inverse Jacobian. Williams and coworkers provide analysis and simulations for planar cable-driven robots in [12]–[14]. Other work in the design and control of fully constrained cable-driven robots includes the WARP [15] and FALCON [16] systems.

Fully constraining a cable-driven robot requires the existence of a strictly positive vector in the left null space of the inverse Jacobian, and the number of cables n must, therefore, exceed the number of DOFs m . Platforms wherein $n = m + 1$ are known as “completely restrained.” Additionally, redundant cables may also be used to increase the workspace or otherwise improve performance.

When $n > m$, the left null space of the inverse Jacobian is nonempty, and there may be an infinite number of valid tension distributions. There exists considerable prior work in determining tension distributions for cable-driven robots with $n = m + 1$. The authors of [17] derive analytical expressions for optimal tension distributions in a completely restrained six-degree-of-freedom (6-DOF) robot, but this method does not extend to redundantly actuated mechanisms. Other previous works [18]–[20] have suggested linear programming (LP) approaches to the problem of determining tension distributions in cable-driven robots.

For redundantly actuated cable-driven robots, prior work in tension distribution is somewhat limited. The authors of

[21] use Dykstra's alternating-projection algorithm to find the minimum-norm tension distributions for a pair of simulated robotic systems. This is an iterative convex optimization method requiring a large number of iterations to converge. The authors of [22] present a noniterative algorithm that computes "safe" and continuous tension distributions for redundant platforms. However, computational complexity scales combinatorially with increasing degrees of actuation redundancy.

It has been shown that tension distributions that are optimal for $\|\cdot\|_p$ are prone to discontinuous behavior for $p = 1, \infty$ [23]. This behavior is characterized by finite step changes in cable tensions resulting from infinitesimally small changes in robot configuration. Such step changes in tension can excite high-frequency oscillation in cables and otherwise degrade system performance. Thus, $\|\cdot\|_1$ or $\|\cdot\|_\infty$ norms should only be used in platforms that do not exhibit discontinuous behavior.

A streamlined calibration process is a requisite for rapid deployability of a field robotic system. While calibration of open-link serial mechanisms has received much attention, calibration of parallel-link systems has been studied only in recent years [24]. Methods to accurately calibrate these systems often require data acquisition from external calibration-specific sensors, such as laser displacement sensors [25] or inclinometers [26]. These sensors can be expensive and significantly complicate setup procedures.

Two more promising technologies are 1) self-calibration, which requires only information gathered by a robot's internal sensors, and 2) autonomous calibration, which requires information from additional joint or link sensors. For both of these methods, sensor redundancy must somehow be introduced. The authors of [24] install a small number of redundant sensors to dynamically calibrate a 6-DOF hexapod machine tool. A hexapod in [27] is locked such that its translational DOFs are removed. Thus, six actuator sensors are used to measure only three DOFs. Another method uses points of singular operation to achieve sensor redundancy [28].

In parallel platforms with redundant links, self-calibration is enabled by the existence of redundant internal sensors. The authors of [29] investigate a number of self-calibration techniques for a 2-DOF robot with three links. A similar platform is considered in [30], but a new error function is proposed that is robust to measurement error of the joint sensors. It should be noted that all of this study is aimed at rigid-arm parallel mechanisms. Although very few examples of prior work exist in the calibration of cable-driven robots, the authors of [31] present self-calibration methods for a biologically inspired cable-driven arm.

In this paper, we present Networked InfoMechanical System for Planar Translation (NIMS-PL), which is a novel 2-DOF four-cable-driven robot designed for actuated sensing in aquatic environments. A schematic of a typical deployment is shown in Fig. 1. Four actuator units are visible, each of which controls one cable. These cables are attached at a common point to an end-effector. While only three cables are required for in-plane translation, a redundant fourth cable is used to enable quadrangular deployment configurations, which increase workspace size and are well suited to typical aquatic configurations. Translation in a planar workspace driven by four cables results in

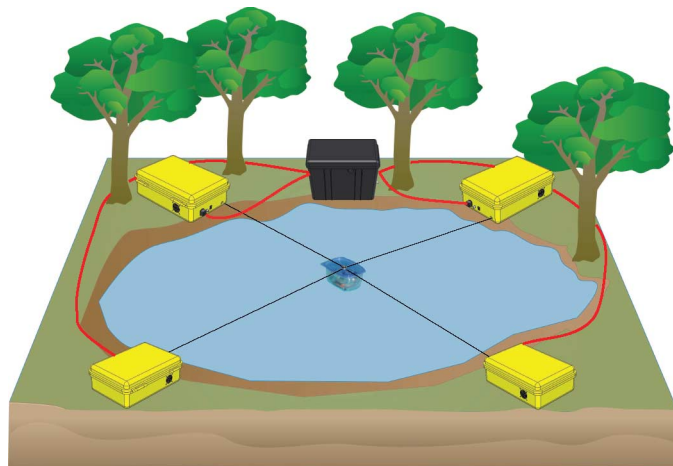


Fig. 1. Schematic of a NIMS-PL deployment showing four actuator units, the motor control box, and a buoyant end-effector.

an infinite set of tension distributions. We have implemented a highly efficient method of computing optimal tension distributions using a specialized LP solver. Furthermore, we have developed two novel methods of self-calibration, which enable the system to measure its own position without external sensors. We also present a least-squares method of monitoring cable slip. This, combined with self-calibration capabilities, is critical in mitigating system drift and enabling long-term autonomous operation.

In summary, the contributions of this paper are as follows:

- 1) design and implementation of a novel 2-DOF cable-driven robot intended for large-scale deployments in aquatic environments;
- 2) highly efficient computation of optimal tension distributions using a specialized LP solver;
- 3) two novel self-calibration methods;
- 4) a least-squares drift-detection algorithm, which is critical in enabling long-term autonomous operation;
- 5) extensive simulation and experimental results showing the performance of our proposed methods.

The remainder of this paper is structured as follows. In Section II, the hardware and software systems comprising NIMS-PL are described. Kinematics are presented in Section III. In Section IV, a brief overview of LP theory is provided and the specialized LP solver used to compute optimal tension distributions is detailed. Thereafter, in Section V, two methods of self-calibration are described and a least-squares drift-detection algorithm is presented. Experimental results are given in Section VI. Finally, in Section VII, we conclude the paper and describe current research objectives.

II. NIMS-PL SYSTEM OVERVIEW

A. System Hardware

The NIMS-PL system consists of four actuation modules, each of which contains a motor–spool assembly, a cantilevered tension sensor, an external encoder, and a spring damper if the actuator is in tension control mode. The design of these individual modules has several advantages. By subdividing the

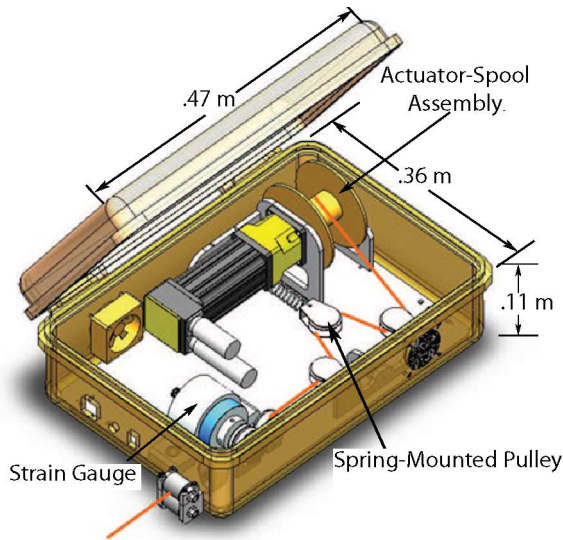


Fig. 2. Actuation module showing the actuator-spool assembly, tension gauge, and spring mounted pulley.

hardware architecture to permit individual modular packages, the size and mass of each case can be reduced. This simplifies transport and installation and enables flexibility in deployment configurations. The modules are designed to be weather and impact resistant, are lightweight and compact, and are housed in robust Pelican brand cases. An actuation module is shown in Fig. 2. These cases can be fixed to the ground or other static fixtures using a combination of stakes and tie-down straps. Alternatively, the cases can be fixed by placing sufficiently heavy items on them.

The actuators are 520 W dc servomotors with built-in 3:1 in-line planetary gearheads. Their peak torque is 3.27 N·m, and the rated speed is 5800 r/min. Thus, they are sufficiently powerful for the large-scale deployments required by many environmental sampling applications.

Precise control of cable release is of paramount importance in this system. Motor position can be controlled by mounting an encoder on the motor output shaft and employing feedback to ensure correct positioning. The critical issue in this system, however, is not controlling motor position but, rather, cable length. Because retraction of the cable into and out of the control modules changes the spooling radius, the relationship between motor position and line release is nonlinear and becomes difficult to predict. Previous work [20] has employed specially designed winch systems in which the cable is wound onto a threaded drum, which moves laterally as the motor rotates. This solution requires substantial hardware complexity and is severely limited in the length of cable that can be stored on the winch. The solution employed in NIMS-PL is to introduce precise cable tracking enabled by optical encoders mounted on idler wheels that rotate freely as the cable passes over them. Since the diameter of the idler wheels is constant, the amount of released cable is directly proportional to the encoder output value and is thereby directly controllable. While the use of these encoders does yield significant improvements in positioning accuracy,

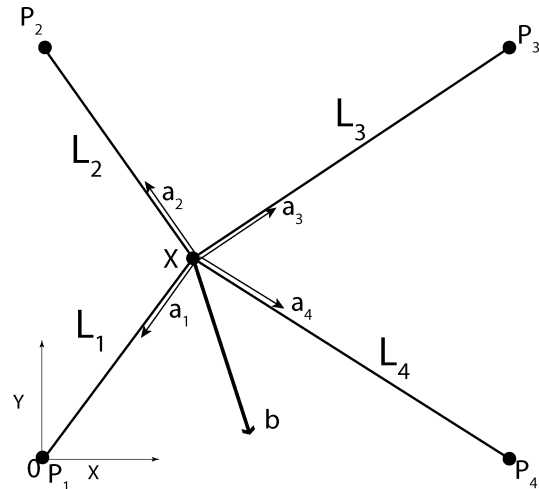


Fig. 3. Schematic of a NIMS-PL configuration showing unit vectors a_i , cable origins P_i , end-effector position $\mathbf{x} = [x \ y]^T$, and an example desired force vector \mathbf{b} .

slippage of a cable relative to an idler wheel is still possible. We have developed novel methods to detect and correct this drift, and these are presented in Section V.

B. Software and Controls

A schematic representation of NIMS-PL is shown in Fig. 3. The lengths of cables 1 and 2 control the position of the end-effector, which is considered a point mass. Motors 3 and 4 are placed in tension control mode, in which they change their respective cable lengths to maintain optimal tensions. The iterative method used to compute optimal tension distributions is presented in Section IV-B. The actuators are controlled by a four-axis controller with integrated pulsewidth-modulated (PWM) amplifiers. Tension control via PID compensation is also managed by this device, with feedback coming from cantilevered strain gauge transducers. In the current system, signal level and motor power lines are routed from the controller to actuator modules. It is important to note that a second configuration also uses fiber-optic communication capabilities for communication between the central controller and the actuation units, while power for each actuation unit is provided locally. This enables synchronized control without necessitating power transmission between the controller and actuator modules.

III. KINEMATICS

Again, consider the schematic shown in Fig. 3. We select P_1 as the origin and P_2 to be on the y -axis. The inverse position kinematics are straightforward, with

$$L_i = \|\mathbf{x} - \mathbf{P}_i\|_2, \quad i = 1, \dots, 4. \quad (1)$$

Using the first two cables to compute position, the forward position kinematics are given by

$$y = \frac{L_1^2 - L_2^2 + y_2^2}{2y_2} \quad (2)$$

and

$$x = \sqrt{L_1^2 - \frac{(L_1^2 - L_2^2 + y_2^2)^2}{4y_2^2}}. \quad (3)$$

The forward velocity kinematics are necessary for the self-calibration method presented in Section V-B; therefore, we provide them here:

$$\begin{aligned} \frac{\partial y}{\partial L_1} &= \frac{L_1}{y_2} \\ \frac{\partial x}{\partial L_1} &= \frac{L_1 (y_2^2 + L_2^2 - L_1^2)}{y_2 \sqrt{4y_2^2 L_1^2 - (y_2^2 + L_1^2 - L_2^2)^2}} \\ \frac{\partial x}{\partial L_2} &= \frac{L_2 (y_2^2 + L_1^2 - L_2^2)}{2y_2^2 \sqrt{L_1^2 - ((y_2^2 + L_1^2 - L_2^2)^2 / 4y_2^2)}} \\ \frac{\partial y}{\partial L_2} &= \frac{-L_2}{y_2}. \end{aligned} \quad (4)$$

IV. EFFICIENT COMPUTATION OF OPTIMAL TENSION DISTRIBUTION

A. Linear Programming Theory

Before describing our method of computing optimal tension distributions, we begin by providing a brief introduction to LP theory. A more complete review of LP theory is available in, for example, [32]. A linear program is one in which the objective is to minimize a linear function subject to linear equality and inequality constraints. Because an equality constraint can be represented as two inequality constraints, it is sufficient to consider only inequalities. Thus, a typical LP problem might be

$$\begin{aligned} p^* &= \min_{\mathbf{r}} \boldsymbol{\lambda}^T \mathbf{r} \\ \text{s.t. } \mathbf{A}_{\text{LP}} \mathbf{r} &\leq \mathbf{b}_{\text{LP}} \end{aligned} \quad (5)$$

where $\mathbf{r} \in \mathbb{R}^h$ is the optimization variable, $\boldsymbol{\lambda} \in \mathbb{R}^h$ is the cost vector, and $\mathbf{A}_{\text{LP}} \in \mathbb{R}^{l \times h}$ and $\mathbf{b}_{\text{LP}} \in \mathbb{R}^l$ represent the inequality constraints. Given such a problem, either 1) the inequality constraints are infeasible, in which case, we define $p^* = \infty$, 2) the problem is unbounded, in which case, $p^* = -\infty$, or 3) the problem is bounded and the feasible region non-empty, in which case, p^* is finite. In any case, the feasible set is an intersection of half-spaces, which is a convex set known as a polyhedron. One property of LPs is that, if the optimal value is finite, an optimal solution p^* always occurs at a basic feasible point. A basic feasible point is one at which the residual, which is given by $\mathbf{b}_{\text{LP}} - \mathbf{A}_{\text{LP}} \mathbf{r}$, is nonnegative and is zero for at least h rows, and the matrix $\hat{\mathbf{A}}$ that contains the rows of \mathbf{A}_{LP} with zero residuals is full-rank.

Every LP has a dual formulation, which we will not discuss here, except that it seeks to maximize a linear objective function $d = \mathbf{b}_{\text{LP}}^T \mathbf{z}$, where \mathbf{z} is the dual variable. In bounded feasible LPs, $d \leq p$, i.e., the objective function of the dual problem is a lower bound for the primal problem. Except for very special cases, the bound is, in fact, tight, and equality occurs only for $d^* = p^*$, corresponding to the optimal solutions of the dual and primal problems, respectively.

A common method used to solve LP problems is the simplex method [33], which jumps from one basic feasible point to another that has a lower objective value. Thus, the simplex method is a descent method, and each iteration has a lower objective value than the previous one. At each iteration, a dual solution is generated, and the corresponding objective value of the dual problem is compared with that of the primal problem. If they are equal, then an optimal solution has been reached.

Because the simplex method is iterative, an initial basic feasible point must be found. This is, in general, nontrivial, and in many cases, a special ‘‘phase 1’’ problem must be solved to generate a starting point for the original problem, which is then referred to as ‘‘phase 2.’’ Thus, two LP problems must be solved.

B. Optimal Tension Distribution

Fig. 3 shows a schematic representation, with cable origins given by $\mathbf{P}_{1,2,3,4}$, end-effector position given by $\mathbf{x} = [x \ y]^T$ and a desired force vector \mathbf{b} that is to be imparted on the end-effector. Hydrodynamic effects and the dynamics of the end-effector and cables can be compensated for by varying \mathbf{b} . This is the subject of future research.

The set of tension distributions that provide the appropriate net force on the end-effector is characterized by

$$\mathbf{A} \mathbf{f} = \mathbf{b} \quad (6)$$

where $\mathbf{f} = [T_1 \ T_2 \ T_3 \ T_4]^T$ is the set of cable tensions, and \mathbf{A} is a pose-dependent structure matrix. The i th column of \mathbf{A} is given by $\mathbf{a}_i = (\mathbf{P}_i - \mathbf{x}) / \|\mathbf{P}_i - \mathbf{x}\|$, which is the unit vector directed from the end-effector \mathbf{x} to \mathbf{P}_i , i.e.,

$$\mathbf{A} = [\mathbf{a}_1 \ \mathbf{a}_2 \ \mathbf{a}_3 \ \mathbf{a}_4]. \quad (7)$$

Since \mathbf{A} is a 2×4 matrix, (6) is underdetermined. Thus, it is apparent that using four cables to control two DOFs results in an infinite number of tension distributions that satisfy the equality condition.

The most significant difference between cable-driven robots and rigid-arm parallel mechanisms is the inability of cables to exert positive or push forces. Thus, to find a valid tension distribution in (6), it becomes necessary to bound the set of tensions between T_{\min} and T_{\max} , which are the lower and upper bounds on tension. The lower bound is required to protect against cable slack, and the upper bound is a result of the finite torque capabilities of the system’s actuators. The optimal tension distribution \mathbf{f}^* can be expressed as follows:

$$\begin{aligned} \mathbf{f}^* &= \underset{\mathbf{f}}{\text{argmin}} \ c(\mathbf{f}) \\ \text{s.t.} & \\ 1) \ \mathbf{A} \mathbf{f} &= \mathbf{b} \\ 2) \ T_{\min} &\leq \mathbf{f} \leq T_{\max} \end{aligned} \quad (8)$$

where $c(\mathbf{f})$ is some cost function. This problem has received some attention in recent years. A completely restrained 6-DOF robot is considered in [17]. The authors find one-norm optimal tensions by reducing the problem to a one-variable LP problem and then exhaustively checking the basic feasible points.

However, this method does not scale well as the degree of dynamic redundancy increases beyond one, because the number of basic feasible points grows rapidly. Furthermore, Verhoeven and Hiller show that one-norm optimal tension distributions are prone to discontinuous behavior [23].

The authors of [21] use Dykstra's alternating projection algorithm to find $\|\cdot\|_2$ optimal tension distributions for a pair of simulated robotic systems. Convergence is slow for this method, and therefore, a large number of iterations must be performed. Furthermore, no experimental results are provided.

As described in Section I, tension distributions that are optimal for either $\|\cdot\|_1$ or $\|\cdot\|_\infty$ are prone to discontinuous behavior. Thus, it must be ensured that platforms using such tension arrangements do not exhibit this behavior. We have learned through extensive experimentation that NIMS-PL does not undergo step tension discontinuities under normal operating conditions. Thus, we select $c(\mathbf{f}) = \|\mathbf{f}\|_1$. In case NIMS-PL has to follow different trajectories than analyzed in these experiments, the continuity can be ensured by offline prechecking or online supervision to stop the system in case of discontinuous tension distributions. To solve (8), we use a specialized version of the standard simplex algorithm [33] that converges on the optimal solution in a very small number of iterations.

We begin by partitioning the structure matrix $\mathbf{A} \in \mathbb{R}^{2 \times 4}$ into two matrices, i.e., \mathbf{B} and $\mathbf{H} \in \mathbb{R}^{2 \times 2}$

$$\mathbf{A} = [\mathbf{B} | \mathbf{H}]. \quad (9)$$

Similarly, we partition the tension vector into two vectors \mathbf{f}_1 and $\mathbf{f}_2 \in \mathbb{R}^2$. Thus

$$\mathbf{A}\mathbf{f} = [\mathbf{B} | \mathbf{H}] \begin{bmatrix} \mathbf{f}_1 \\ \mathbf{f}_2 \end{bmatrix} = \mathbf{b}. \quad (10)$$

Solving for \mathbf{f}_2 yields

$$\mathbf{f}_2 = \mathbf{H}^{-1}(\mathbf{b} - \mathbf{B}\mathbf{f}_1) \quad (11)$$

and the objective function $c(\mathbf{f})$ becomes

$$c(\mathbf{f}) = \|\mathbf{f}\|_1 = \mathbf{1}^T(\mathbf{f}_1 + \mathbf{H}^{-1}(\mathbf{b} - \mathbf{B}\mathbf{f}_1)) \quad (12)$$

where $\mathbf{1}$ is a vector of ones.

Equation (8) becomes

$$\begin{aligned} \mathbf{f}_1^* &= \underset{\mathbf{f}_1}{\operatorname{argmin}} \mathbf{1}^T(\mathbf{f}_1 + \mathbf{H}^{-1}(\mathbf{b} - \mathbf{B}\mathbf{f}_1)) \\ \text{s.t.} & \\ 1) & T_{\min} \leq \mathbf{f}_1 \leq T_{\max} \\ 2) & T_{\min} \leq \mathbf{H}^{-1}(\mathbf{b} - \mathbf{B}\mathbf{f}_1) \leq T_{\max}. \end{aligned} \quad (13)$$

The original four-variable LP, which had an equality constraint, has been reduced to a two-variable LP without an equality constraint.

This LP must be solved by the controller during the kinematics routines, and the solver must, therefore, be implemented in an efficient way. We employ a novel adaptation of the simplex algorithm, in which we select $\mathbf{f}_1 = [T_{\min} \ T_{\min}]^T$ as an initial starting point, since we know it is an intersection of two edges. There is no guarantee that this starting point is feasible, but if this is the case, it is the optimal operating point. If one or more

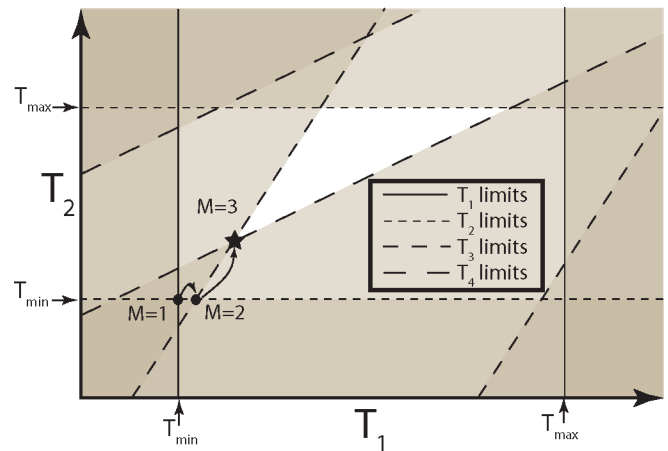


Fig. 4. Example of the iterative tension solver. For iteration number $M = 1$, $\mathbf{f}_1 = [T_{\min} \ T_{\min}]^T$, but two constraints are violated. The next point is found by moving along the $T_2 = T_{\min}$ edge toward the first violated constraint. After this iteration, only one violated constraint remains, and we move along the T_3 constraint to the optimal operating point \mathbf{f}_1^* .

inequality constraints is violated, we select the first violated constraint k , and move toward it along the edge that approaches constraint k fastest. We move along the edge until we reach the closest intersection. This is repeated until either a feasible point is found or it is determined that the feasible set is empty. The feasible set is found to be empty if it is not possible to move closer to constraint k along either of the active edges. Extensive experimental evaluation on NIMS-PL has shown that, if a feasible point is found, it is always the optimal solution. Thus, our method does not require a two-phase solution.

If our algorithm is applied to other robotic configurations, in which the first feasible point may not be optimal, it is of interest to find an upper bound on the number of iterations N required of a second-phase simplex solver. Generating tight upper bounds on N is not generally possible [34], but N must always be lower than the number of extreme points P of the feasible polyhedron. Upper bounding P is also difficult, and furthermore, P grows quickly with increasing problem dimensions. However, for configurations wherein the number of cables n exceeds the number of DOFs m by exactly 2, $P \leq 2n$. Thus, given that the first phase has found a suboptimal extreme point of a feasible polyhedron with the maximum number of extreme points $2n$, the worst-case behavior would be that the simplex algorithm foregoes an initially adjacent optimal point and must circumvent the entire polyhedron. In this case, the number of iterations required would be $2n - 1$. Thus, if $n = m + 2$, the number of iterations required for a second-phase is upper bounded by $2n - 1$. For NIMS-PL, this yields a maximum of seven iterations for convergence from a suboptimal starting point. It should, however, be noted that the simplex algorithm is typically characterized by much faster convergence and that it would be difficult to contrive a scenario in which this upper bound is met. This is particularly true when our adaptation of the simplex algorithm is used to find near-optimal starting points.

An example of our simplex method is shown in Fig. 4. Because (13) is a two-variable LP, we can represent the problem

TABLE I

ITERATIONS REQUIRED FOR CONVERGENCE FOR FEASIBLE OPERATION POINTS

Number of Iterations	1	2	3	4
Probability	.246	.410	.307	.037

TABLE II

ITERATIONS REQUIRED FOR CONVERGENCE FOR INFEASIBLE OPERATION POINTS

Number of Iterations	1	2	3	4
Probability	.248	.410	.335	.008

graphically with T_1 on the horizontal axis and T_2 on the vertical axis. There are eight constraints in (13) (two for each cable), and these are represented as half-spaces, with the infeasible region shown in gray. The feasible region is the intersection of the feasible half-spaces and is shown in white. The starting point, with iteration number $M = 1$, is $\mathbf{f}_1 = [T_{\min} \ T_{\min}]^T$. The next point is found by moving along the $T_2 = T_{\min}$ edge toward the first violated constraint. After this iteration, only one violated constraint remains, and we move along the T_3 constraint to the optimal operational point \mathbf{f}_1^* .

It is generally not possible to provide tight upper bounds on the number of iterations required to solve LP problems using active-set algorithms [34]. The number of iterations is always upper bounded by the total number of intersections of constraints R , because the optimal solution lies at one of these intersections, and each intersection is visited at most once. However, as the dimensionality of the problem increases, R grows combinatorially, and this upper bound becomes trivial. However, for very small-scale problems, R remains reasonable. For NIMS-PL, in which there are four sets of parallel 2-D hyperplanes: $R = 24$. Thus, the number of iterations required to compute the optimal tension distribution or prove infeasibility in NIMS-PL is always bounded by 24. However, use of our novel adaptation of the simplex algorithm, combined with our selection of $[T_{\min} \ T_{\min}]^T$ as a starting point, yields significantly faster convergence.

Because it is not possible to provide tight upper bounds on the number of iterations required for convergence, we must demonstrate the efficiency of our algorithm statistically. We consider a hypothetical configuration with anchor points at the vertices of a square with sides of length 10 m. The desired force vector \mathbf{b} is taken to be 10 N with a random direction, and we take $T_{\min} = 10$ N and $T_{\max} = 100$ N. The optimal tension distribution was computed for 10 000 randomly chosen locations, and the number of iterations required for convergence was recorded. The results are shown in Table I, which shows the probability associated with each iteration number for feasible points, and Table II, which shows the number of iterations required to prove infeasibility in the case of infeasible operation points. In the former case, the average number of iterations is 2.13, and in the latter, it is 2.10. It is apparent that only a small fraction of the 24 potential constraint intersections are considered. Furthermore, floating point operation (FLOP)-count analysis of the simplex algorithm shows that each iteration requires fewer than 100 FLOPs. Thus, in the worst case encountered in our simulations, the computational cost of computing \mathbf{f}^* was less than 400 FLOPs, which is quite small for modern CPUs.

V. SELF-CALIBRATION

The actuation redundancy resulting from in-plane translation driven by four cables results in redundant sensors, thereby enabling self-calibration, which is essential for rapid deployments and long-term autonomous operation. For example, during a deployment, the field team may wish to freely spool out cables and connect them to an end-effector in the workspace. Thereafter, the system would be powered up, but would have no information regarding position. Calibration would then require some sort of measurement device, which may be expensive or require significant training. Furthermore, as is the case with any dead-reckoning system, drift may accumulate over time, thus resulting in significant positioning error. As discussed in Section V-C, redundant cables enable detection of this error, and self-calibration enables its correction.

We have developed two novel self-calibration methods that enable the system to discover its current position with no prior information regarding cable lengths. The first method uses high-fidelity tension gauges that are already in place for tension control, whereas the second method uses small moves or jitters to determine the position.

It should be noted that these calibration methods assume that the locations of the anchor points \mathbf{P}_i , $i = 1, \dots, 4$ are known. In a deployment, these locations can be found by measuring distances between the points using a laser rangefinder and computing the locations consistent with these measurements.

A. Tension-Based Self-Calibration

At static equilibrium, we have

$$\mathbf{A}(\mathbf{x})\mathbf{f} = 0 \quad (14)$$

where we have included \mathbf{x} to emphasize that the matrix \mathbf{A} is indeed a function of position. If the position is held constant and the tension distribution is changed by some amount $\Delta\mathbf{f} \in \mathbb{R}^4$, then we have

$$\mathbf{A}(\mathbf{x})\Delta\mathbf{f} = 0. \quad (15)$$

Thus, we propose the following self-calibration scheme, where we use the notation given in Fig. 3.

- 1) The lengths of cables 3 and 4 are held constant, while cable 1 increases its tension by some amount ΔT_1 , and cable 2 maintains steady tension.
- 2) The resulting tension distribution $\tilde{\mathbf{f}}_1$ is recorded.
- 3) The system returns to its original tension distribution \mathbf{f}_0 .
- 4) The lengths of cables 3 and 4 are again held constant, while cable 2 increases its tension by some amount ΔT_2 , and cable 1 maintains steady tension.
- 5) The resulting tension distribution $\tilde{\mathbf{f}}_2$ is recorded.
- 6) The system returns to its original tension distribution \mathbf{f}_0 .

It should be noted here that without any prior knowledge of end-effector position, it is impossible to find an initial tension distribution \mathbf{f}_0 , which is guaranteed to meet the constraints imposed by (8). To resolve this issue, we use this calibration method only if we can assure that the end-effector is near the center of the workspace. Furthermore, the initial tensions in cables 1 and 2 are set to $1.5 \times T_{\min}$ so that the resulting

tensions in cables 3 and 4 do not approach slack conditions. In our experiments, $\Delta T_1 = \Delta T_2 = 1.5 \times T_{\min}$. However, if one of the cables approaches slack conditions during the transition to the new tension distributions, the tension transition is halted, and the corresponding tension distribution is measured at that operating point.

We now define

$$\Delta \mathbf{F} = [\tilde{\mathbf{f}}_1 - \mathbf{f}_0 | \tilde{\mathbf{f}}_2 - \mathbf{f}_0]. \quad (16)$$

From (15), we have

$$\mathbf{A}(\mathbf{x})\Delta \mathbf{F} = 0 \quad (17)$$

and finding the position \mathbf{x}^* can be expressed as

$$\mathbf{x}^* = \underset{\mathbf{x}}{\operatorname{argmin}} \|\mathbf{A}(\mathbf{x})\Delta \mathbf{F}\|_F^2 \quad (18)$$

where we are using the Frobenius norm. We compute \mathbf{x}^* online by means of an iterative Newton method [34].

B. Jitter-Based Self-Calibration

The jitter-based calibration method uses small changes in the lengths of cables 1 and 2 and the resulting changes in cables 3 and 4 to compute position, where we again use the notation given in Fig. 3. In short, we experimentally determine the ratio of the changes in cable lengths $\Delta L_i / \Delta L_j$, for $i = 3, 4$ and $j = 1, 2$ and then find the position \mathbf{x} that is most consistent with these measurements.

In order to experimentally determine $\Delta L_i / \Delta L_j$ for $i = 3, 4$ and $j = 1, 2$, we proceed as follows.

- 1) Place cables 3 and 4 in tension control mode, such that they maintain a constant tension.
- 2) While keeping L_2 constant, make a small change ΔL_1 in L_1 , and record the resulting changes ΔL_{31} and ΔL_{41} in the lengths of cables 3 and 4.
- 3) Return cable 1 to its original length.
- 4) While keeping L_1 constant, make a small change ΔL_2 in L_2 , and record the resulting changes ΔL_{32} and ΔL_{42} in the lengths of cables 3 and 4.
- 5) Return cable 2 to its original length.

We can now compute a matrix of experimental partial derivatives $\Delta \mathbf{L}_{\text{exp}}$

$$\Delta \mathbf{L}_{\text{exp}} = \begin{bmatrix} \frac{\Delta L_{31}}{\Delta L_1} & \frac{\Delta L_{32}}{\Delta L_2} \\ \frac{\Delta L_{41}}{\Delta L_1} & \frac{\Delta L_{42}}{\Delta L_2} \end{bmatrix}. \quad (19)$$

The forward velocity kinematics, which is given in (4), provide expressions for $\partial x / \partial L_1$, $\partial y / \partial L_1$, $\partial x / \partial L_2$, and $\partial y / \partial L_2$. We can find expressions for $\partial L_i / \partial L_j$ for $i = 3, 4$ and $j = 1, 2$ as follows:

$$\frac{\partial L_i}{\partial L_j} = \frac{\partial L_i}{\partial x} \frac{\partial x}{\partial L_j} + \frac{\partial L_i}{\partial y} \frac{\partial y}{\partial L_j}, \quad i = 3, 4, \quad j = 1, 2 \quad (20)$$

where $\partial L_i / \partial x = (x - x_i) / L_i$, and $\partial L_i / \partial y = (y - y_i) / L_i$. We can now compute the matrix of partial derivatives $\mathbf{dL}(\mathbf{x})$

$$\mathbf{dL}(\mathbf{x}) = \begin{bmatrix} \frac{\partial L_3}{\partial L_1} & \frac{\partial L_3}{\partial L_2} \\ \frac{\partial L_4}{\partial L_1} & \frac{\partial L_4}{\partial L_2} \end{bmatrix} \quad (21)$$

where we again include the \mathbf{x} term to emphasize that $\mathbf{dL}(\mathbf{x})$ is a function of position. The position \mathbf{x}^* most consistent with the measured partial derivatives $\Delta \mathbf{L}_{\text{exp}}$ is given by

$$\mathbf{x}^* = \underset{\mathbf{x}}{\operatorname{argmin}} \|\mathbf{dL}(\mathbf{x}) - \Delta \mathbf{L}_{\text{exp}}\|_F^2. \quad (22)$$

We compute \mathbf{x}^* online by means of a direct multidirectional search method discussed in [35].

C. Drift Detection

Once the system has performed self-calibration, the lengths of all cables can be determined by means of inverse kinematics. Initially, all cable lengths will agree perfectly with one another. However, as drift accumulates during operation, we expect the agreement between the cable lengths to decrease. A least-squares time-of-arrival (TOA) method [36] can be used to detect this drift. Given the four cable origins $\mathbf{P}_i = [x_i \ y_i]^T$ and cable lengths L_i , $i = 1, \dots, 4$, we have

$$L_i = \sqrt{(x - x_i)^2 + (y - y_i)^2}, \quad i = 1, \dots, 4. \quad (23)$$

By squaring both sides and rearranging, we arrive at

$$x_i x + y_i y - 0.5R^2 = \frac{1}{2}(x_i^2 + y_i^2 - L_i^2), \quad i = 1, \dots, 4 \quad (24)$$

where $R = \sqrt{x^2 + y^2}$. Equation (24) can be written as

$$\mathbf{\Lambda} \Theta = \mathbf{g} \quad (25)$$

where

$$\mathbf{\Lambda} = \begin{bmatrix} x_1 & y_1 & -\frac{1}{2} \\ \vdots & \vdots & \vdots \\ x_4 & y_4 & -\frac{1}{2} \end{bmatrix}, \quad \Theta = \begin{bmatrix} x \\ y \\ R^2 \end{bmatrix} \quad (26)$$

$$\mathbf{g} = \frac{1}{2} \begin{bmatrix} x_1^2 + y_1^2 - L_1^2 \\ \vdots \\ x_4^2 + y_4^2 - L_4^2 \end{bmatrix}.$$

In the presence of error in cable lengths, the position of the end-effector can now be estimated using the standard least-squares approximation

$$\hat{\Theta} = (\mathbf{\Lambda}^T \mathbf{\Lambda})^{-1} \mathbf{\Lambda}^T \mathbf{g}. \quad (27)$$

The residual, which is given by $(\mathbf{\Lambda} \hat{\Theta} - \mathbf{g})^T (\mathbf{\Lambda} \hat{\Theta} - \mathbf{g})$, is a measure of how well the cable lengths agree with one another. A small residual indicates that the cable lengths agree well and that little drift has occurred, whereas a large residual indicates that drift has occurred. Thus, if the residual rises above some threshold, a self-calibration routine is run, after which, the system resumes operation.

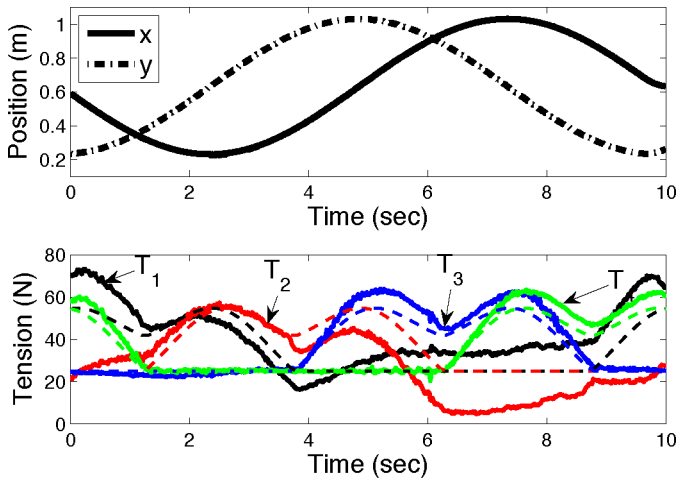


Fig. 5. Experimental tension distribution results showing cable tensions and end-effector position during execution of a circular trajectory. Commanded tensions are shown as dashed lines.

VI. EXPERIMENTAL RESULTS

In order to provide experimental validation of our methods, we performed an indoor deployment of a vertical configuration in our laboratory. The size of the workspace was $1.264 \text{ m} \times 1.264 \text{ m}$, and the end-effector was small enough to be considered massless.

A. Tension Distribution Experiments

In order to evaluate the performance of the tension distribution algorithm, tensions were monitored while a circular trajectory was executed. The circle was centered at the middle of the workspace, with $\mathbf{x} = [0.632 \ 0.632]^T \text{ m}$, and had a radius of 0.40 m . The resulting tension traces are shown in Fig. 5, along with x and y traces. For these trials, $T_{\min} = 20 \text{ N}$, and $T_{\max} = 100 \text{ N}$.

The trajectory begins and ends near the edge between motors 1 and 4 and moves clockwise. At the initial point, cables 1 and 4 are required to maintain high tensions to balance the forces of cables 2 and 3. As the trajectory moves toward the edge between motors 1 and 2 ($t = 2.5 \text{ s}$), these cables become taut, and cable 4 becomes slack. At $t = 5 \text{ s}$, cables 2 and 3 become taut as the trajectory nears the edge between these motors. At $t = 7.5 \text{ s}$, cables 3 and 4 become taut, and as the trajectory approaches the starting point, cables 1 and 4 again become taut. It is apparent that the tension distribution algorithm successfully avoids slack conditions throughout execution of the trajectory, despite low tension in cable 2 between $t = 6 \text{ s}$ and $t = 9 \text{ s}$. This temporary violation of tension constraints, which is caused by imperfect tension regulation, underscores the importance of positive, nonzero, lower tension limits.

B. Self-Calibration Experiments

In order to experimentally verify the performance of our proposed calibration methods, both routines were performed at a set of positions within the workspace of a laboratory-scale $1.264 \text{ m} \times 1.264 \text{ m}$ deployment. For the jitter-based method,

TABLE III
AVERAGE CALIBRATION ERROR

Method	Tension	Jitter
Avg. Error (cm)	1.98	.63

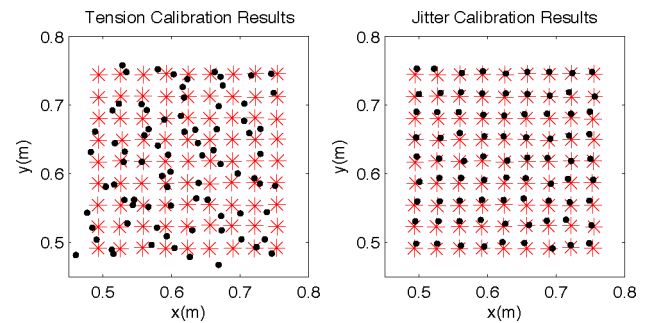


Fig. 6. Calibration results for (left) tension-based and (right) jitter-based calibration methods. Stars indicate actual position, while dots show calibration results.

the length of the jitter was taken to be 0.038 m or 3% of the workspace size. A video camera was used to monitor the actual position throughout the experiment. Thereafter, the calibration results were compared with the corresponding positions as found by image processing of the video camera data.

The set of points considered was a square 9×9 grid spanning the center of the workspace from 0.5 to 0.75 m . The calibration results for both methods are given in Table III. The average error for the tension-based method was 1.98 cm , whereas the error for the jitter-based method was 0.63 cm . It is apparent that the jitter-based method offers significantly improved accuracy as compared with the tension-based scheme. It should be noted here that the image-processing equipment used to verify location in these experiments was limited to a resolution of 0.3 cm per pixel. Thus, the accuracy of the jitter-based method closely approaches the resolution of our measurement device.

Fig. 6 shows the calibration results for both methods. Stars indicate actual position, and dots show calibration results. Because the average error achieved by the tension-based method is comparable with the distance between experimental points, it is difficult to discern which tension-based calibration result corresponds to a particular experimental point. However, for the jitter-based method, the average error is low, and the correspondence is close.

The jitter-based calibration scheme is characterized by improved accuracy and reduced susceptibility to force disturbances, thus making it better suited for most applications. However, the tension-based method is preferable in situations where moving the end-effector during calibration is not possible. For example, the user may wish to calibrate the system while the end-effector is sampling some phenomenon and must remain stationary for some time. In other situations, the time required to perform a jitter is prohibitive. In these cases, the tension-based method might be preferable.

It should be noted here that these results demonstrate successful operation only for a laboratory-scale workspace. The effects of nonidealities such as cable sag, which may affect performance in larger workspaces, are the subject of current research.

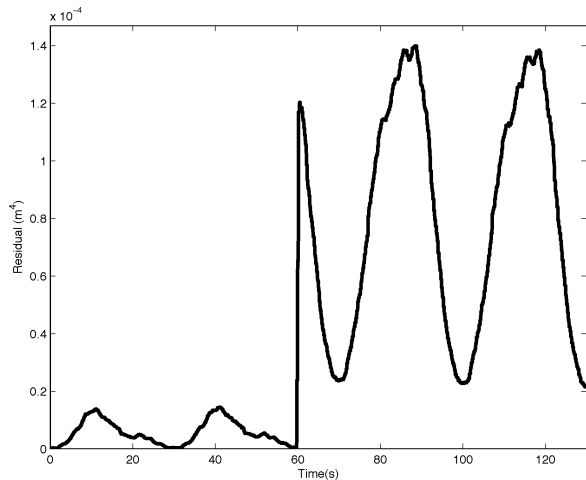


Fig. 7. Trace of the residual from the drift-detection algorithm during execution of a circular trajectory. At $t = 59.5$ s, a drift of 2.44 cm is introduced in the length of cable 4.

C. Drift-Detection Experiments

Our proposed cable drift-detection algorithm is intended to mitigate the effects of drift and, thereby, enable long-term autonomous operation. However, this drift occurs over long periods of time, and it is difficult to demonstrate long-term drift correction experimentally. In order to provide results of drift detection within a reasonable time span, we artificially introduce drift by obscuring the LED on the optical encoder regulating cable 4. While the light is obscured, the encoder registers zero movement, and the controller's estimate of cable length becomes inaccurate.

During our experiments, the end-effector was moved in a circle of radius 0.2 m centered at the middle of a 1.264 m \times 1.264 m workspace. In the first trial, a 2.44-cm drift was introduced in L_4 at time $t = 59.5$ s. A trace of the resulting residual is shown in Fig. 7. Initially, a small residual is evident. This residual is due to imperfections in the measurements of the cable origins and in the initial calibration. The residual is also a function of position within the workspace, as is evidenced by its periodic oscillation as the end-effector executes its circle. However, when drift is introduced in L_4 , the magnitude of the residual increases. Thus, with appropriate thresholding, the drift can be successfully detected.

Once cable drift has been detected, it is necessary to correct the drift to improve positioning accuracy. In order to demonstrate this drift correction, a similar experiment was performed in which a 12.3-cm drift was introduced in L_4 at time $t = 20$ s during execution of a circular trajectory. NIMS-PL immediately detects the drift but waits for the completion of its current circle, at which point, it self-calibrates and resumes operation. A trace of L_4 during this experiment is shown in Fig. 8. Before the drift is introduced, L_4 oscillates sinusoidally, as is expected during execution of a circular trajectory. Once drift has occurred, a considerable offset is observed in L_4 during the completion of the final circle. Thereafter, NIMS-PL performs jitter-based self-calibration, during which, L_4 experiences a slight change as a result of the jitter at $t = 38$ s. At $t = 52$ s, NIMS-PL re-

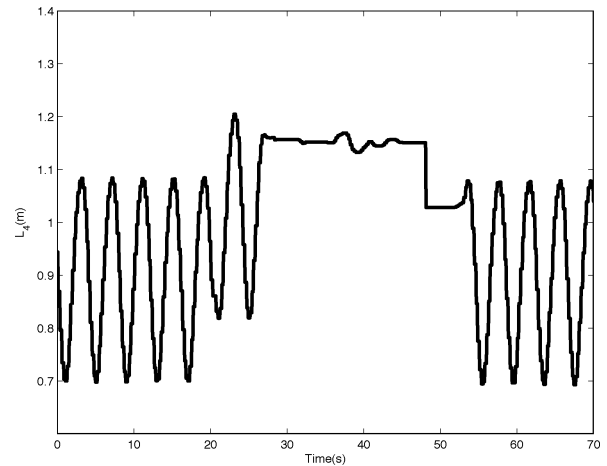


Fig. 8. Trace of L_4 showing a large offset caused by cable drift and subsequent drift correction via jitter-based self-calibration.

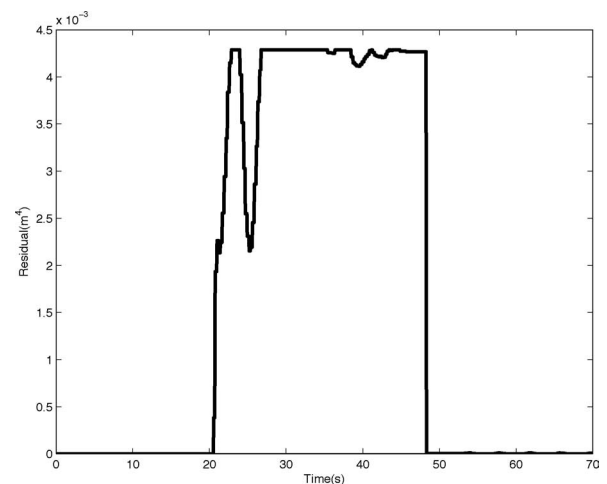


Fig. 9. Trace of drift-detection residual during the drift-correction experiment.

sumes execution of the circular trajectory. It is apparent that the drift in L_4 has been virtually eliminated, as the original 12.3 cm offset has been reduced to 0.3 cm. The drift-detection residual during this experiment is shown in Fig. 9. The large residual caused by the introduction of drift is reduced from 4.3×10^{-3} to 7.8×10^{-6} .

VII. CONCLUSION

In this paper, we have introduced NIMS-PL, which is a novel 2-DOF cable-driven robotic system intended for aquatic sensing applications. The actuation redundancy resulting from in-plane translation driven by four cables results in an infinite number of cable tension distributions. We propose a novel, highly efficient, iterative algorithm and demonstrate its efficiency in simulation and experiments on a laboratory-scale NIMS-PL deployment.

We have also proposed two novel self-calibration methods. The accuracy of these calibration schemes has been verified experimentally by means of video imaging tests, and the applicability of each calibration method to various deployment situations is described.

A least-squares drift-detection algorithm has been developed to enable long-term autonomous operation. We have experimentally verified the ability of this algorithm to detect small amounts of cable drift. Furthermore, we have performed experiments demonstrating the ability of NIMS-PL to significantly reduce error by performing self-calibration upon detection of drift.

There are many planned applications for NIMS-PL in actuated sensing of aquatic environments. This includes monitoring of stream, river, reservoir, and lake systems. Current research is directed to performing in-field deployments in regions of interest to the scientific community.

REFERENCES

- [1] A. Riechel, P. Bosscher, H. Lipkin, and I. Ebert Uphoff, "Concept paper: Cable-driven robots for use in hazardous environments," in *Proc. 10th Int. Top. Meeting Robot. Remote Syst. Hazardous Environ.*, Mar. 2004, pp. 310–316.
- [2] F. Takemura, M. Enomoto, T. Tanaka, K. Denou, Y. Kobayashi, and S. Tadokoro, "Development of the balloon-cable driven robot for information collection from sky and proposal of the search strategy at a major disaster," in *Proc. IEEE/ASME Int. Conf. Adv. Intell. Mechatronics*, Jul. 2005, pp. 658–663.
- [3] F. Takemura, K. Maeda, and S. Tadokoro, "Attitude stability of a cable driven balloon robot," in *Proc. IEEE/RSJ Int. Conf. Intell. Robots Syst.*, Oct. 2007, pp. 3504–3509.
- [4] SkyCam. (2007). [Online]. Available: www.skycam.tv
- [5] CableCam. (2007). [Online]. Available: www.cablecam.com
- [6] K. Usher, G. Winstanley, P. Corke, D. Stauffacher, and R. Carnie, "Air vehicle simulator: An application for a cable array robot," in *Proc. IEEE Int. Conf. Robot. Autom.*, Apr. 2005, pp. 2241–2246.
- [7] B. Jordan, M. Batalin, and W. Kaiser, "NIMS RD: A rapidly deployable cable based robot," in *Proc. IEEE Int. Conf. Robot. Autom.*, Apr. 2007, pp. 144–150.
- [8] T. Harmon, R. Ambrose, R. Gilbert, J. Fisher, M. Stealey, and W. Kaiser, "High-resolution river hydraulic and water quality characterization using rapidly deployable networked infomechanical systems (NIMS RD)," *Environ. Eng. Sci.*, vol. 24, pp. 151–159, 2006.
- [9] A. Singh, M. A. Batalin, M. J. Stealey, V. Chen, Y. Lam, M. Hansen, T. Harmon, G. Sukhatme, and W. J. Kaiser, "Mobile robot sensing for environmental applications," in *Field and Service Robotics*. Berlin, Germany: Springer, Jun. 2007, pp. 125–135.
- [10] A. Singh, M. Batalin, V. Chen, M. Stealey, B. Jordan, J. Fisher, T. H. ad M. Hansen, and W. Kaiser, "Autonomous robotic sensing experiments at san Joaquin river," in *Proc. IEEE Int. Conf. Robot. Autom.*, Apr. 2007, pp. 4987–4993.
- [11] R. G. Roberts, T. Graham, and T. Lippit, "On the inverse kinematics, statics, and fault tolerance of cable-suspended robots," *J. Robot. Syst.*, vol. 15, no. 10, pp. 581–597, 1998.
- [12] R. L. Williams and P. Gallina, "Planar cable-direct-driven robots, part i: Kinematics and statics," presented at the ASME Des. Tech. Conf., Pittsburgh, PA, Sep. 2001.
- [13] R. L. Williams, P. Gallina, and A. Rossi, "Planar cable-direct-driven robots, Part II: Dynamics and control," presented at the ASME Des. Tech. Conf., Pittsburgh, PA, Sep. 2001.
- [14] R. L. Williams, P. Gallina, and J. Vadia, "Planar translational cable-driven robots," *J. Robot. Syst.*, vol. 20, pp. 107–120, 2003.
- [15] K. Maeda, S. Tadokoro, T. Takamori, M. Hiller, and R. Verhoeven, "On design of a redundant wire-driven parallel robot warp manipulator," in *Proc. Int. Conf. Robot. Autom.*, May 1999, pp. 895–900.
- [16] S. Kawamura, W. Choe, S. Tanaka, and S. Pandian, "Development of an ultrahigh speed robot falcon using wire drive system," in *Proc. IEEE Int. Conf. Robot. Autom.*, 1995, pp. 215–220.
- [17] S. Fang, D. Franitz, M. Torlo, F. Bekes, and M. Hiller, "Motion control of a tendon-based parallel manipulator using optimal tension distribution," *IEEE/ASME Trans. Mechatron.*, vol. 9, no. 3, pp. 561–568, Sep. 2004.
- [18] W. Shiang, D. Cannon, and J. Gorman, "Dynamic analysis of the cable array robotic crane," in *Proc. IEEE Int. Conf. Robot. Autom.*, May 1999, vol. 4, pp. 2495–2500.
- [19] W. Shiang, D. Cannon, and J. Gorman, "Optimal force distribution applied to a robotic crane with flexible cables," in *Proc. IEEE Int. Conf. Robot. Autom.*, Apr. 2000, vol. 2, pp. 1948–1954.
- [20] C. Pham, G. Yang, and S. Yeo, "Dynamic analysis of cable-driven parallel mechanisms," in *Proc. IEEE/ASME Int. Conf. Adv. Intell. Mechatron.*, Jul. 24–28, 2005, pp. 612–617.
- [21] M. Hassan and A. Khajepour, "Minimum-norm solution for the actuator forces in cable-based parallel manipulators based on convex optimization," in *Proc. IEEE Int. Conf. Robot. Autom.*, Apr. 2007, pp. 1498–1503.
- [22] L. Mikelsons, T. Bruckmann, M. Hiller, and D. Schramm, "A real-time capable force calculation algorithm for redundant tendon-based parallel manipulators," in *Proc. IEEE Int. Conf. Robot. Autom.*, May 2008, pp. 3869–3874.
- [23] R. Verhoeven and M. Hiller, "Tension distribution in tendon-based Stewart platforms," presented at the ARK 8th Int. Symp. Adv. Robot Kinematics, Bagnaux, France, 2002.
- [24] H. Zhuang, L. Liu, and O. Masonry, "Autonomous calibration of hexapod machine tools," *J. Manuf. Sci. Eng.*, vol. 122, pp. 140–148, Feb. 2000.
- [25] A. Goswami, A. Quaid, and M. Peshkin, "Complete parameter identification of a robot from partial pose information," in *Proc. IEEE Int. Conf. Robot. Autom.*, 1993, vol. 1, pp. 168–173.
- [26] S. Besnard and W. Khalil, "Calibration of parallel robots using two inclinometers," in *Proc. IEEE Int. Conf. Robot. Autom.*, 1999, pp. 1758–1763.
- [27] A. Rauf and J. Ryu, "Fully autonomous calibration of parallel manipulators by imposing position constraint," in *Proc. IEEE Int. Conf. Robot. Autom.*, May 2001, pp. 2389–2394.
- [28] P. Last, D. Schutz, A. Raatz, and J. Hesselbach, "Singularity based calibration of 3-dof fully parallel planar manipulators," presented at the 12th IFToMM World Congr., Besançon, France, Jun. 2007.
- [29] Y. Yiu, J. Meng, and Z. Li, "Auto-calibration for a parallel manipulator with sensor redundancy," in *Proc. Int. Conf. Robot. Autom.*, Sep. 2003, vol. 3, pp. 3660–3665.
- [30] Y. Zhang, S. Cong, Z. Li, and S. Jiang, "Auto-calibration of a redundant parallel manipulator based on the projected tracking error," *Arch. Appl. Mech.*, vol. 77, pp. 697–706, Mar. 2007.
- [31] S. K. Mustafa, G. Yang, S. H. Yeo, W. Lin, and I. M. Chen, "Self-calibration of a biologically-inspired 7-DOF cable-driven robotic arm," *IEEE Trans. Mechatronics*, vol. 13, no. 1, pp. 66–75, Feb. 2008.
- [32] D. Bertsimas and J. Tsitsiklis, *Introduction to Linear Programming*. Belmont, MA: Athena Scientific, 1997.
- [33] G. Dantzig, A. Orden, and P. Wolfe, "Generalized simplex method for minimizing a linear form under linear inequality constraints," *Pac. J. Math.*, vol. 5, no. 2, pp. 183–195, 1955.
- [34] S. Boyd and L. Vandenberghe, *Convex Optimization*. Cambridge, U.K.: Cambridge Univ. Press, 2004.
- [35] M. H. Wright, "Direct search methods: Once scorned, now respectable," presented at the Dundee Biennial Conf. Numer. Anal., Dundee, U.K., 1996.
- [36] K. Cheung, H. So, W. Ma, and Y. Chan, "Least squares algorithms for time-of-arrival-based mobile location," *IEEE Trans. Signal Process.*, vol. 52, no. 4, pp. 1121–1127, Apr. 2004.



Per Henrik Borgstrom received the B.S. and M.S. degrees in electrical engineering in 2005 and 2007, respectively, from the University of California at Los Angeles, where he is currently working toward the Ph.D. degree in electrical engineering.

He is engaged in research on the design of cabled robotic platforms for use in actuated sensing applications.



Brett L. Jordan received the B.S. and M.S. degrees in mechanical engineering from the University of California at Los Angeles (UCLA), in 2006 and 2008, respectively.

He is currently a Staff Research Engineer at UCLA, where he is involved in mechanical design and product development.



Bengt J. Borgstrom (M'08) received the B.S. and M.S. degrees in electrical engineering in 2004 and 2005, respectively, from the University of California at Los Angeles (UCLA), where he is currently working toward the Ph.D. degree in electrical engineering.

He is also with the Speech Processing and Auditory Perception Laboratory, UCLA. His current research interests include speech processing, specifically noise robust recognition, audiovisual speech processing, distributed speech recognition,

and speech coding.



Michael J. Stealey received the B.S. degree in computer science and the M.S. degree in electrical engineering from the University of California at Los Angeles (UCLA).

He is currently with UCLA. He is also a Senior Research Software Developer with the Renaissance Computing Institute, Chapel Hill, NC.



Gaurav S. Sukhatme (S'94–M'97–SM'05) received the M.S. and Ph.D. degrees in computer science from the University of Southern California (USC), Los Angeles.

He is currently an Associate Professor of computer science (joint appointment in electrical engineering) with USC, where he is also the Codirector of the Robotics Research Laboratory and the Director of the Robotic Embedded Systems Laboratory, which he founded in 2000. His current research interests include multirobot systems, sensor/actuator networks,

and robotic sensor networks. He has authored or coauthored extensively in these and related areas. He is the Editor-in-Chief of *Autonomous Robots*.

Prof. Sukhatme was a recipient of the National Science Foundation (NSF) CAREER Award and the Okawa Foundation Research Award. He was a Principle Investigator (PI) on several NSF, Defense Advanced Research Projects Agency, and National Aeronautics and Space Administration Grants. He is a Co-PI with the Center for Embedded Networked Sensing, which is an NSF Science and Technology Center. He is a member of the Association for the Advancement of Artificial Intelligence and the Association for Computing Machinery. He is one of the founders of the Robotics: Science and Systems Conference. He was the Program Chair of the 2008 IEEE International Conference on Robotics and Automation. He was an Associate Editor of the *IEEE TRANSACTIONS ON ROBOTICS* and the *IEEE TRANSACTIONS ON MOBILE COMPUTING*. He is member of the Editorial Board of *IEEE Pervasive Computing*.



Maxim A. Batalin (S'03–M'05) received the M.S. and Ph.D. degrees in computer science from the University of Southern California, Los Angeles, in 2002 and 2005, respectively.

He is currently a Researcher with the Center for Embedded Networked Sensing, University of California at Los Angeles, where he joined the Wireless Health Program in 2005 at the Actuated, Sensing, Coordinated and Embedded Networked Technologies Laboratory and managed the development of the first of its kind incremental diagnosis method

for biomedical applications that allows accurate patient state identification with minimum sensor usage. His current research interests include the research, design, and implementation of systems in the areas of robotics, sensors, general biomedical computing, and system integration. He has also managed the development of the first end-to-end wireless health monitoring system, i.e., MEDIC, which offers a wireless, wearable architecture for biomedical data acquisition, local processing, and transmittal to a remote enterprise server. He is the author or coauthor of more than 35 conference and journal publications in the areas of wireless health, mobile robotics, sensor networking, actuated sensor systems, biomedical systems, environmental sampling, and others. He also has expertise in the development of software systems for mobile wireless platforms.

Dr. Batalin is a member of the Sigma Xi.



William J. Kaiser (M'95–SM'00) received the Ph.D. degree in solid-state physics from Wayne State University, Detroit, MI, in 1984.

From 1977 through 1986, he was a Research Staff with Ford Motor Company, where he was involved in the development of automotive sensor and embedded system technology that resulted in large volume commercial sensor production. He also developed the first spectroscopies directed to microelectronics systems based on scanning tunneling microscopy. From 1986 through 1994, he was with the Jet Propulsion Laboratory,

Pasadena, CA, where he initiated the National Aeronautics and Space Administration (NASA) Microinstrument Program for distributed sensing. In 1994, he joined the Department of Electrical Engineering, University of California at Los Angeles (UCLA), where he initiated the first wireless networked microsensor programs with a vision of linking the Internet to the physical world through distributed monitoring. His current research interests include low-power embedded computing for wireless networked sensing, biomedical embedded computing, robotic sensor systems for environmental monitoring, and distributed sensing for energy and water resource management. He has authored or coauthored more than 170 publications and holds 23 patents.

Prof. Kaiser was the Chairman of the Department of Electrical Engineering at UCLA from 1996 through 2000. He received the Peter Mark Award from the American Vacuum Society, the NASA Medal for Exceptional Scientific Achievement, the Arch Colwell Best Paper Award from the Society of Automotive Engineers, the Best Paper Award at BodyNets 2008, two R&D 100 Awards, the Allied Signal Faculty Research Award, the Brian P. Copenhaver Award for Innovation in Teaching with Technology, and the UCLA Gold Shield Faculty Award.